An Efficient and Robust I-f Control of Sensorless IPMSM With Large Startup Torque Based on Current Vector Angle Controller

Zhihao Song, *Student Member, IEEE*, Wenxi Yao, *Member, IEEE*, Kevin Lee, *Fellow, IEEE*, and Wuhua Li, *Member, IEEE*

***Abstract*—Interior permanent magnet synchronous motor (IPMSM) with back electromotive-force (EMF) based sensorless field-oriented control (FOC) is widely used in medium-high speed applications. Unfortunately, the back EMF is too small to be estimated accurately during low speed operation. Hence, the current-frequency (*I–f*) control with controllable current vector is used for startup. However, the conventional *I–f* control is hard to realize the tradeoff between startup speed and load capacity, suffering high-acceleration and high-load startup failure. In this article, a current vector angle controller for sensorless IPMSM startup is proposed to adjust speed-up-stage current acceleration and constant-speed-stage current amplitude with load automatically. The proposed angle controller guarantees the current vector angle close to the maximum torque per ampere angle, which contributes to large startup torque, high operating efficiency and smooth transition from *I–f* startup to sensorless FOC. Furthermore, the robustness against parameters variation of angle controller is evaluated quantitatively. These theoretical advantages are verified in experiments with a 380 V, 1.5 kW IPMSM. In particular, the experimental results demonstrate that the proposed *I–f* control realizes full-load startup even with ±50% flux linkage and ±30% inductance variation. Furthermore, the startup acceleration auto-adjusts with load to reconcile startup speed and load capacity.**

***Index Terms*—Current vector angle controller, current-frequency (*I–f*) control, interior permanent magnet synchronous motor (IPMSM), sensorless control, startup strategy.**

I. Introduction

RECENTLY, the usage of permanent magnet synchronous motors (PMSMs) has increased in industrial applications due to their appealing features, such as high power density, high efficiency, robust rotor structure, and low maintenance cost [1]. In order to improve operation performance, PMSM requires accurate and real-time rotor position, which is traditionally achieved by installing speed sensor, such as incremental encoder [2] or resolver [3]. However, these sensors reduce system reliability in harsh working conditions and increase overall cost and volume [4]. Therefore, robust sensorless control strategies are more preferred, which can be roughly classified into two categories [5]: the back electromotive-force (EMF) estimation methods [6]–[9] for medium-high speed applications and the signal injection methods [10]–[12] for medium-low speed applications. In order to achieve high performance over the entire speed range, the back EMF estimation method adapted to medium-high speed needs to be combined with a signal injection method for startup and low speed operation [13], which obviously complicates the overall control algorithm. In most applications, PMSMs do not operate at ultra-low speed except during startup. Therefore, the advantages of signal injection methods such as good dynamic response at low speed are insignificant compared to its disadvantages, such as complexity, loss, torque fluctuations and high noise. Desirably, a simple and effective startup strategy is more suitable than signal injection method to accelerate the motor to a speed where the back EMF is high enough for accurate estimation.

The *V/f* control widely used in induction motor is introduced into PMSMs and various improved *V/f* control methods have been proposed. Although the stability and efficiency of *V/f* control are improved by frequency correction [14] and amplitude correction [15], [16], the overall performance of open current loop *V/f* control is still far inferior than field-oriented control (FOC). Furthermore, due to different control structures and principles of operation, it is not always trouble free to transit from *V/f* control to FOC after initial startup.

Another simple and effective startup strategy is known as the current-frequency (*I–f*) control, which has closed-loop current regulator and thus solves the problem of uncontrolled current in *V/f* control. The startup process under *I–f* control can be divided into three main stages including speed up, constant speed and transition to sensorless FOC [17]. Due to the low damping coefficient of PMSM itself, the damping ratio needs to be increased to improve system stability, which can be realized by frequency correction based on active power perturbations [18], [19]. The stability analysis and parameter design based on linearized motion model have been discussed in [20].

Manuscript received 9 March 2022; revised 30 May 2022; accepted 8 July 2022. Date of publication 25 July 2022; date of current version 6 September 2022. This work was supported in part by the National Nature Science Foundation of China under Grant 52077197 and in part by the Zhejiang Intelligent Electrical Manufacturing Innovation Center. Recommended for publication by Associate Editor M. Hartmann. (*Corresponding author: Wenxi Yao.*)

Zhihao Song, Wenxi Yao, and Wuhua Li are with the College of Electrical Engineering, Zhejiang University, Hangzhou 310027, China (e-mail: songzhihao@zju.edu.cn; ywxi@zju.edu.cn; woohualee@zju.edu.cn).

Kevin Lee is with Eaton Corporation, Milwaukee, WI 53216 USA (e-mail: kevinlee@eaton.com).

Color versions of one or more figures in this article are available at https://doi.org/10.1109/TPEL.2022.3193565.

Digital Object Identifier 10.1109/TPEL.2022.3193565

During speed up stage, various frequency increasing modes of current vector are used, such as $f \propto t$ [17], $f \propto t^2$ [21], and $f \propto (1 - \cos\omega t)$ [22]. However, there is no closed-loop frequency controller in these methods, which means the acceleration needs to be set relatively small to avoid losing synchronization during heavy-load startup. Actually, the acceleration should be adjusted with load. In [19], the acceleration is generated by a torque controller, which makes the output torque equal to a constant and large value.

After accelerating to the set speed, the current frequency remains constant while the current amplitude gradually decreases to improve efficiency and ensure a smooth transition to sensorless FOC. Similarly, the current amplitude should be adjusted with load. Using instantaneous reactive power feedback to adjust the current amplitude, the $i_d = 0$ control for surface PMSM is realized in [20] and the maximum torque per ampere (MTPA) control for interior PMSM (IPMSM) is realized in [23]. Additionally, a current oriented *I–f* control with a closed-loop angle regulator design based on Lyapunov theory is proposed for MTPA realization [24].

Another key technique is the transition strategy from *I–f* startup to sensorless FOC. The smooth transition is achieved by a first-order lag compensator in [21]. A simple current cross-over technique is introduced, but is limited to light-load startup condition [25]. In [26], the output of position estimator and speed PI regulator are further processed by an adaptive compensator to generate suitable current amplitude and angle for smooth transition.

Generally speaking, the load capacity, startup speed and efficiency are the common requirements of *I–f* control, but the existing methods have shortcomings to achieve an optimal tradeoff among them. Actually, these requirements can be naturally satisfied once the motor runs at MTPA state during three startup stages. However, lacking of accurate current angle information and corresponding angle control, the MTPA state under *I–f* control is particularly unstable. The stability can be enhanced by leaving some angle margin. For IPMSM, the current vector angle under MTPA state is slightly less than zero. Thus, sacrificing a little bit of efficiency, the id = 0 operation, i.e., regulating current vector angle to zero, is adopted for higher stability margin, which achieves a good performance tradeoff. Hence, an angle controller is proposed in this article. Its input is the current vector angle, i.e., the angle error between current vector and q-axis, which can be easily obtained through current oriented voltage equation. During speed up stage, the current amplitude is set to the rated value for large startup torque while the current acceleration is the output of angle controller. Thus, the acceleration will be automatically adjusted with load to minimize angle error. Once the angle error is zero, the output torque is constant and large, which obviously shortens the acceleration period. After reaching the set speed, the current frequency remains constant while the current amplitude is the output of angle controller. Similarly, the angle controller will make angle error near zero by adjusting current amplitude with load. The core idea of the proposed angle controller is to maintain the angle error close to zero throughout the whole startup process, which ensures large startup torque, high efficiency and smooth transition from *I–f* control to sensorless FOC. Moreover, this proposed *I–f* control has strong robustness because the angle error estimation is insensitive to parameter variations. So, this fast, efficient and robust *I–f* control has high practical value, even if the load is heavy during startup process.

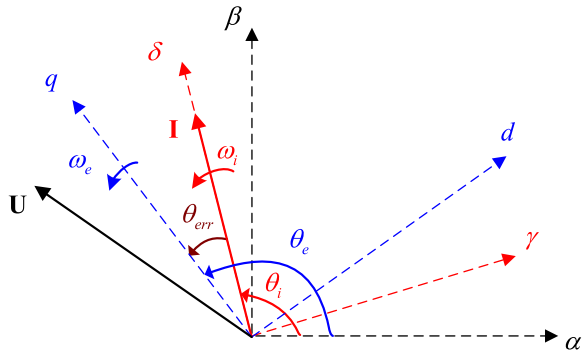

Fig. 1. Vector diagram including dq and $\gamma\delta$ frames for IPMSM.

II. Mathematical IPMSM Model With *I–f* Control

The voltage equations in the dq coordinate system are

$$u_d = R_s i_d + L_d \frac{d}{dt} i_d - \omega_e L_q i_q \tag{1}$$

$$u_q = R_s i_q + L_q \frac{d}{dt} i_q + \omega_e L_d i_d + \omega_e \lambda_f \tag{2}$$

where u_d and u_q represent d-axis and q-axis voltages, respectively, i_d and i_q denote d-axis and q-axis currents respectively, R_s, L_d, L_q, λ_f and ω_e represent stator resistance, d-axis inductance, q-axis inductance, permanent magnet flux linkage and electrical angular, velocity respectively.

However, in practical applications, the *I–f* startup method is used in cases where the actual angle position is not known due to unreliable position signal or lack of a position sensor. Therefore, the actual dq coordinate frame is not known. In *I–f* control, the current vector is fully controllable. In order to analyze the characteristics of current vector, the $\gamma\delta$ coordinate system oriented by the current vector is introduced in Fig. 1.

The coordinate systems $\alpha\beta$ and dq are stationary and synchronous frames, respectively. The δ-axis is aligned with the current vector **I**, the angle between current vector **I** and α axis is denoted by θ_i, and the angle between q-axis and α-axis is denoted by θ_e. The angle between current vector **I** and q axis is θ_{err}, satisfying $\theta_{\text{err}} = \theta_e - \theta_i$. The frequencies ω_i and ω_e represent current vector and motor angular velocities respectively.

Since the angle error between q-axis and δ-axis is θ_{err}, the voltage equations in the $\gamma\delta$ coordinate system are

$$u_\gamma = R_s i_\gamma + L_d \frac{d}{dt} i_\gamma - \omega_i L_q i_\delta - \omega_e \lambda_f \sin\theta_{\text{err}} \tag{3}$$

$$u_\delta = R_s i_\delta + L_q \frac{d}{dt} i_\delta + \omega_i L_d i_\gamma + \omega_e \lambda_f \cos\theta_{\text{err}} \tag{4}$$

where u_γ and u_δ represent γ-axis and δ-axis voltages, respectively, i_γ and i_δ denote γ-axis and δ-axis currents, respectively.

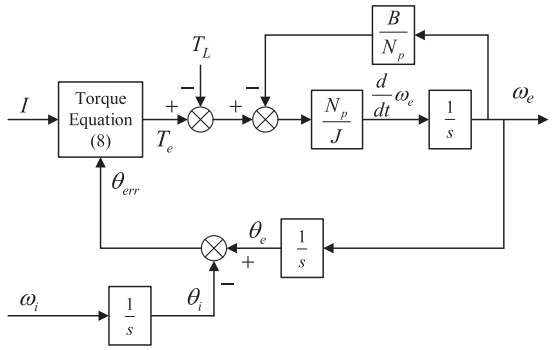

Fig. 2. Large-signal motion model of IPMSM under *I–f* control.

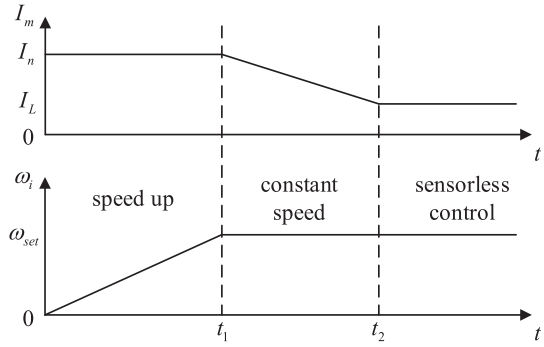

Fig. 3. Current vector amplitude and speed of conventional *I–f* control.

Since δ-axis is aligned with the current vector **I**, the currents satisfy $i_\gamma = 0$, $i_\delta = I_m$, where I_m is the amplitude of current vector **I**. Then the $\gamma\delta$-axis voltage equations can be simplified as [23]

$$u_\gamma = -\omega_i L_q i_\delta - \omega_e \lambda_f \sin\theta_{\text{err}} \tag{5}$$

$$u_\delta = R_s i_\delta + L_q \frac{d}{dt} i_\delta + \omega_e \lambda_f \cos\theta_{\text{err}}. \tag{6}$$

According to the relationship between dq and $\gamma\delta$ coordinate systems, the derivative of angle error can be obtained as

$$\frac{d}{dt}\theta_{err} = \frac{d}{dt}(\theta_e - \theta_i) = \omega_e - \omega_i. \tag{7}$$

The torque equation of IPMSM is

$$\begin{aligned} T_e &= 1.5 N_p i_q [\lambda_f + (L_d - L_q) i_d] \\ &= 1.5 N_p I_m \cos\theta_{\text{err}} [\lambda_f + (L_d - L_q) I_m \sin\theta_{\text{err}}] \end{aligned} \tag{8}$$

where the currents satisfy $i_q = I_m \cos\theta_{\text{err}}$, $i_d = I_m \sin\theta_{\text{err}}$, and N_p is number of pole pairs.

The motor motion equation is

$$\frac{J}{N_p}\frac{d}{dt}\omega_e = T_e - T_L - \frac{B}{N_p}\omega_e \tag{9}$$

where J is moment of inertial, T_L is load torque and B is damping coefficient.

Since the current response is fast enough compared to the motion response, the actual current vector can be regarded the same as the given current vector of current regulator when considering the motion state. Then, combined with motion (9), torque (8) and angle error (7), the large-signal motion model of IPMSM under *I–f* control can be obtained as shown in Fig. 2.

III. Performance Analysis of Conventional *I–f* Startup Method

The conventional *I–f* startup method can be divided into three stages. During the speed up stage, the current vector amplitude is maintained constant as rated value while the current vector frequency ω_i increases with time. When the speed reaches the set value, the motor switches to constant speed stage, where the current vector frequency is maintained constant and the current amplitude decreases gradually. As the current amplitude decreases, the angle error θ_{err} between current vector and q-axis decreases as well. When the angle error θ_{err} decreases to a relatively small value, the strategy switches to sensorless FOC. The current vector amplitude and frequency of conventional *I–f* control during the entire startup sequence are shown in Fig. 3.

However, there are problems in the conventional *I–f* startup strategy, such as speed oscillation caused by low damping ratio and losing synchronization during speed up stage. This section mainly analyzes these two issues.

TABLE I
Tested IPMSM Parameters

Parameter	Value	Parameter	Value
Rated power P_n	1.5 kW	Resistance R_s	4.8 Ω
Rated voltage V_n	380 Vrms	d-axis inductance L_d	31.5 mH
Rated current I_n	2.7 Arms	q-axis inductance L_q	92.3 mH
Rated speed n	1500 rpm	Pole pairs N_p	3
Rated torque T_n	9.55 Nm	Flux linkage λ_f	0.67 Wb
Inertia J	0.019 kgm^2	Damping coefficient B	0.015 Nms

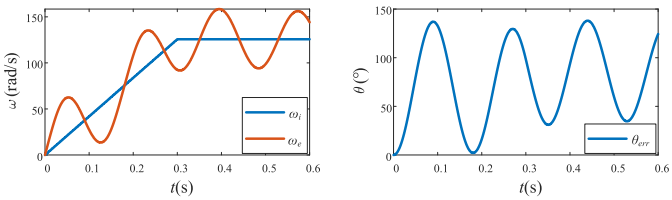

Fig. 4. Speed and angle error under conventional *I–f* control at no load.

A. Speed Oscillation Caused By Low Damping Ratio

The motor parameters are given in Table I, where the damping coefficient B is relatively small. After applying the current vector in Fig. 3 to the large-signal motion model in Fig. 2, the speed and angle error under *I–f* control at no load are recorded in Fig. 4. Clearly, in this case, the speed and angle errors oscillate in a great deal. The detailed stability analysis can be referred to [20].

In order to solve the speed oscillation caused by low damping ratio, a frequency correction method based on active power fluctuation is proposed in [18]. The correction frequency $\Delta\omega_i$ of current vector is proportional to the derivative of motor operating frequency $\frac{d}{dt}\omega_e$, i.e.,

$$\Delta\omega_i = \omega_i - \omega_{i0} = -k_{dp}\frac{d}{dt}\omega_e \tag{10}$$

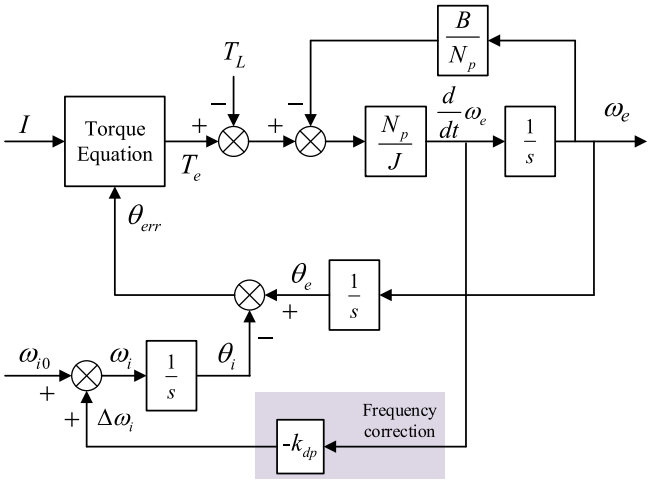

Fig. 5. Large-signal motion model under *I–f* control with frequency correction.

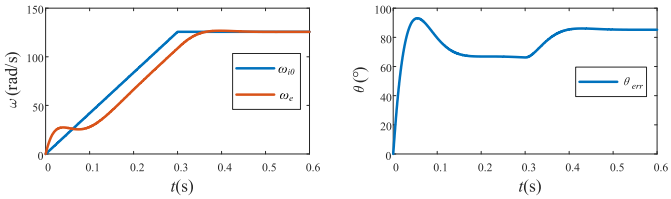

Fig. 6. Speed and angle error under *I–f* control with frequency correction at no load.

where ω_{i0} and ω_i are current vector frequency without and with frequency correction respectively. The gain k_{dp} for damping is a positive constant. The derivative of motor frequency can be obtained through high-pass filtering of the active power. The specific derivation process and parameter selection will be described in detail in the following section.

With frequency correction (10), the large-signal motion model under *I–f* control can be obtained as shown in Fig. 5, and the speed and angle error at no load are recorded in Fig. 6. In this case, there are no speed oscillation and the motor frequency ω_e lags behind the set current vector frequency ω_i. This is because the system equivalent damping ratio is increased by the frequency correction.

B. Losing Synchronization During Speed Up Stage

Under conventional *I–f* control, the motor often loses synchronization especially during high-load or high-acceleration startup. This is because the output torque cannot reach the demand torque, which needs to be quantitatively analyzed. According to the motion (9), the demand torque with load T_L and acceleration $\beta = \frac{d}{dt}\omega_e$ satisfies

$$T_d = T_L + \frac{B}{N_p}\omega_e + \frac{J}{N_p}\beta\,. \tag{11}$$

Obviously, the larger the load T_L or acceleration β is, the larger the demand torque T_d is.

According to torque (8), the motor output torque T_e with respect to angle error θ_{err} is recorded in Fig. 7. When the motor

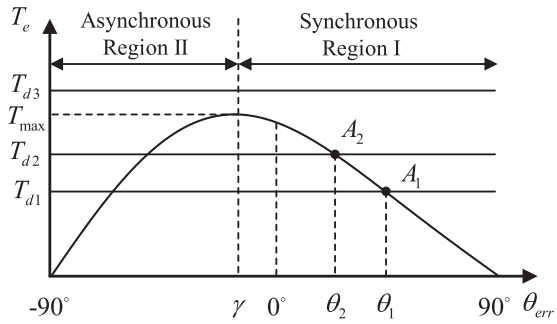

Fig. 7. Variation of generated torque with angle error.

runs at MTPA state, the output torque T_e reaches its maximum value $T_{\max}$, and the present angle error θ_{err} is equal to the MTPA angle γ, which satisfies

$$\gamma = \sin^{-1}\frac{\lambda_f - \sqrt{\lambda_f^2 + 8(L_d - L_q)^2 I^2}}{4(L_q - L_d)\,I} < 0. \tag{12}$$

Based on whether the angle error θ_{err} is greater than the MTPA angle γ, the operating region can be divided into synchronous region I and asynchronous region II as shown in Fig. 7. When load T_L increases suddenly, the angle error θ_{err} will decrease according to (9). Then, in synchronous region I, as the angle error θ_{err} decreases, the output torque T_e will increase. When it increases to the demand torque T_d, the motor will be stable again. However, in asynchronous region II, as the angle error θ_{err} decreases, the output torque T_e will decrease, and thus the angle error θ_{err} will further decrease according to (9), which makes motor lose synchronization. Therefore, it is necessary to ensure the motor runs in synchronous region I. Furthermore, when the motor runs in region I, if the demand torque increases from T_{d1} to T_{d2}, the steady-state operating point will switch from point A_1 to A_2 accordingly as shown in Fig. 7. However, when the demand torque increases to T_{d3}, which is larger than the maximum output torque $T_{\max}$, the operating point keeps moving to the left. Once it enters asynchronous region II, the motor will lose synchronization.

With the same acceleration in Fig. 6 and at full load, the speed, angle error and torque are recorded in Fig. 8. When the demand torque T_d is less than maximum torque $T_{\max}$, the steady-state operating point is always in synchronous region I, where the output torque T_e gradually approaches the demand torque T_d. However, according to (11), when the load T_L and acceleration β are large, as the speed ω_e increases, the demand torque T_d may be larger than the maximum torque $T_{\max}$, leading to the loss of synchronization. It can be seen more intuitively from the angle error waveform that once the angle error θ_{err} is smaller than MTPA angle γ, the operating point enters asynchronous region II and thus the angle error θ_{err} keeps on decreasing, resulting in loss of synchronization and startup failure.

Therefore, the conventional *I–f* startup method suffers from losing synchronization as described and thus an improved method is needed to refine the *I–f* control.

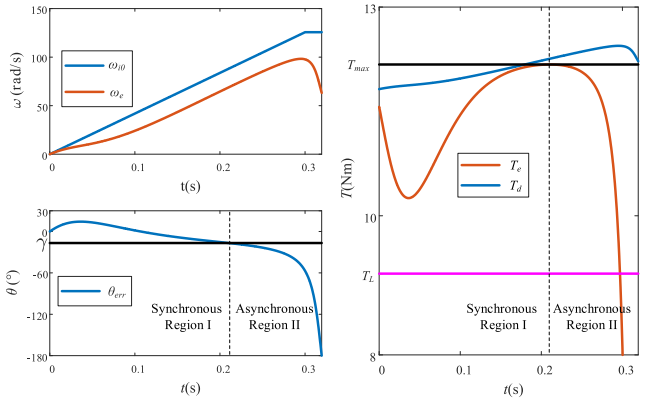

Fig. 8. Speed, angle error and torque under *I–f* control with frequency correction at full load.

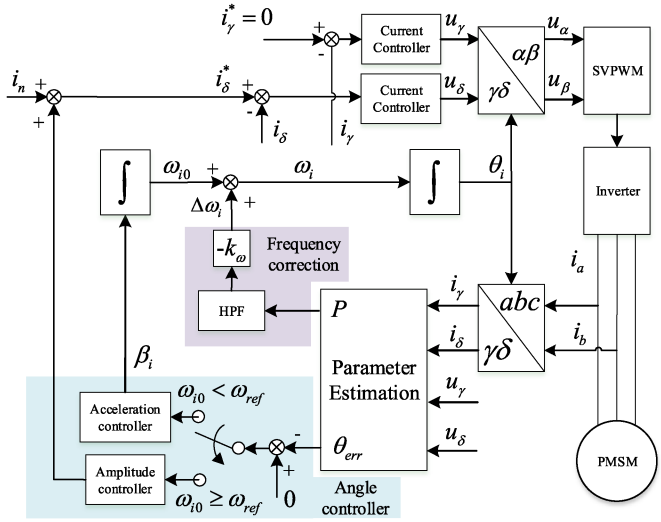

Fig. 9. Proposed *I–f* startup method with angle controller.

IV. Proposed *I–f* Startup Method Based on Angle Controller

From previous analysis, it is clear that the motor can lose synchronization when the demand torque T_d is greater than the maximum output torque $T_{\max}$ during speed up stage. According to (11), the demand torque T_d mainly consists of the load torque T_L and the acceleration torque $\frac{J}{N_p}\beta$ for speeding up with acceleration β. Since the load torque is determined by external working condition, the controllable torque is the acceleration torque. Therefore, the demand torque T_d can be controlled by adjusting acceleration β to be smaller than the maximum output torque $T_{\max}$. In other words, when the load torque T_L is large, the demand torque T_d can be avoided from exceeding $T_{\max}$ by decreasing acceleration β. In fact, it follows from Fig. 7 that maintaining $T_d < T_{\max}$ is essential to keep $\theta_{err} > \gamma$. Therefore, the demand torque T_d can be ensured smaller than the maximum torque $T_{\max}$ by controlling $\theta_{\text{err}} = 0$ to avoid the loss of synchronization. When $\theta_{\text{err}} = 0$, the output startup torque is relatively large and close to its maximum value $T_{\max}$.

When the motor accelerates to the set speed and switches to constant speed stage, the acceleration β is zero, causing demand torque T_d to decrease sharply according to (11). If the motor current remains unchanged, the angle error θ_{err} will increase significantly as demand torque T_d decreases according to Fig. 7, which reduces the operating efficiency. In order to improve efficiency, it is necessary to reduce motor current and $T_{\max}$, thus the angle error θ_{err} will decrease. Similarly, the angle error θ_{err} needs to be larger than the MTPA angle γ to avoid losing synchronization. Therefore, the motor current can be adjusted to maintain $\theta_{\text{err}} = 0$, which not only realizes high efficiency, but also facilitates subsequent smooth transition to sensorless FOC on the premise of avoiding losing synchronization.

Combined with the previous analysis, an improved *I–f* startup method based on angle controller is proposed as shown in Fig. 9. The core idea of the proposed method is to adjust the acceleration of current vector during speed up stage and adjust the amplitude of current vector during constant speed stage to maintain angle error $\theta_{\text{err}} = 0$. Thus, throughout the whole *I–f* startup process, the angle error θ_{err} is guaranteed to be zero, which ensures large startup torque, high efficiency and smooth transition to subsequent sensorless FOC.

Since the torque equation in large-signal motion model shown in Fig. 2 is nonlinear, the performance analysis and controller design are both complicated. Therefore, by linearizing the torque (8), the small-signal model of torque equation can be obtained as

$$\Delta T_e = K_I \cdot \Delta I \ - K_\theta \cdot \Delta\theta_{\text{err}} \tag{13}$$

where K_I and K_θ are small-signal gains, satisfying

$$K_I = \frac{\partial T_e}{\partial I} = \frac{3}{2}N_p\left[(L_d - L_q)\, I\sin 2\theta_{\text{err}} + \lambda_f \cos\theta_{\text{err}}\right] \tag{14}$$

$$K_\theta = -\frac{\partial T_e}{\partial \theta_{\text{err}}} = \frac{3}{2}N_p\left[(L_q - L_d)\, I^2\cos 2\theta_{err} + \lambda_f I\cos\theta_{\text{err}}\right]. \tag{15}$$

Very often, in order to guarantee a very small initial θ_{err}, the rotor position initialization is carried out before *I–f* startup, such as applying a fixed current vector to align the rotor [20] or detecting the initial position through high frequency pulsating voltage injection [27]. After startup, the proposed angle controller works to bring the angle error θ_{err} to zero. Therefore, the steady-state angle error θ_{err} is close to zero during *I–f* startup. So the small-signal gains (14) and (15) can be simplified as

$$K_I = \frac{\partial T_e}{\partial I}\Big|_{\,\theta_{err}=0} = \frac{3}{2}N_p\lambda_f \tag{16}$$

$$K_\theta = -\frac{\partial T_e}{\partial \theta_{err}}\Big|_{\,\theta_{\text{err}}=0} = \frac{3}{2}N_p\,(L_q - L_d)\, I^2. \tag{17}$$

Combined with small-signal torque (13), the small-signal motion model in Fig. 10 can be derived from large-signal motion model shown in Fig. 2.

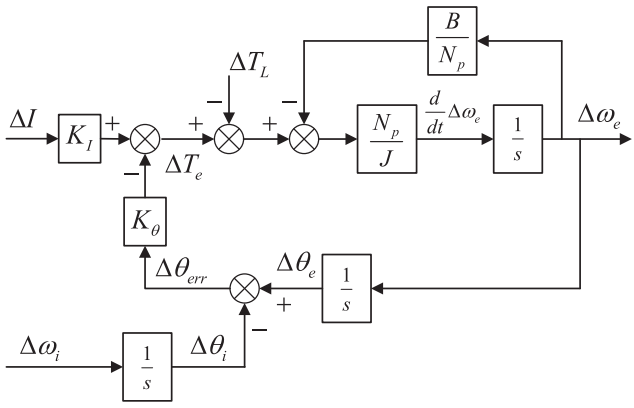

Fig. 10. Small-signal motion model of IPMSM under *I–f* control.

The small-signal angle error (18) and motion (19) as below are derived from (7) and (9), respectively,

$$\Delta\theta_{\text{err}} = \frac{1}{s}(\Delta\omega_e - \Delta\omega_i) \tag{18}$$

$$\Delta\omega_e = \frac{N_p}{sJ+B}(\Delta T_e - \Delta T_L). \tag{19}$$

Combing (13), (18), and (19), the relationship among small-signal angle error $\Delta\theta_{\text{err}}$, current amplitude ΔI, current frequency $\Delta\omega_i$ and load torque ΔT_L can be derived as

$$\Delta\theta_{\text{err}} = G_{\theta I}\Delta I + G_{\theta\omega}\Delta\omega_i + G_{\theta T}\Delta T \tag{20}$$

where the transfer functions satisfy

$$G_{\theta I} = \frac{N_p K_I}{s^2 J + sB + N_p K_\theta} \tag{21}$$

$$G_{\theta\omega} = -\frac{sJ+B}{s^2 J + sB + N_p K_\theta} \tag{22}$$

$$G_{\theta T} = -\frac{N_p}{s^2 J + sB + N_p K_\theta}. \tag{23}$$

Based on the above transfer functions, the sections below analyze how to control the current vector amplitude I and frequency ω_i to make the angle error θ_{err} converge to zero stably and quickly.

A. Frequency Correction Design

According to transfer functions (21)–(23), the characteristic equation of the system under *I–f* control is

$$s^2 J + sB + N_p K_\theta = 0. \tag{24}$$

The damping ratio ζ of the characteristic (24) is

$$\zeta = \frac{B}{2\sqrt{JN_p K_\theta}} \tag{25}$$

According to the motor parameters in Table I, it can be seen that the damping coefficient B is relatively small, so the system damping ratio ζ is small, leading to large speed oscillation during startup stage as shown in Fig. 4. In order to solve the speed oscillation caused by low damping ratio, a frequency correction method is proposed in [19]. The equation of correction frequency $\Delta\omega_i$ satisfies (10) and the corresponding small-signal equation is expressed as

$$\Delta\omega_i = \Delta\omega_{i0} - k_{dp}\frac{d}{dt}\Delta\omega_e \tag{26}$$

where $\Delta\omega_{i0}$ and $\Delta\omega_i$ are current vector frequency perturbations without and with frequency correction respectively, and $\Delta\omega_e$ is motor frequency perturbation. Substituting (26) into (18), the angle error θ_{err} with frequency correction can be obtained as

$$\Delta\theta_{\text{err}} = \frac{1}{s}\left[(1+sk_{dp})\,\Delta\omega_e - \Delta\omega_{i0}\right]. \tag{27}$$

Combining (13), (19), and (27), the transfer functions with frequency correction are derived as

$$G'_{\theta I} = \frac{N_p K_I(sk_{dp}+1)}{s^2 J + sB_e + N_p K_\theta} \tag{28}$$

$$G'_{\theta\omega} = -\frac{sJ+B}{s^2 J + sB_e + N_p K_\theta} \tag{29}$$

$$G'_{\theta T} = -\frac{N_p(sk_{dp}+1)}{s^2 J + sB_e + N_p K_\theta} \tag{30}$$

where B_e is the equivalent damping coefficient with frequency correction and satisfies

$$B_e = B + N_p K_\theta k_{dp} \approx N_p K_\theta k_{dp}\ (B \ll N_p K_\theta k_{dp}). \tag{31}$$

Comparing the transfer functions (21)–(23) and (28)–(30), it's noteworthy that with frequency correction, the equivalent damping coefficient increases from B to B_e. To obtain faster convergence with less oscillation, the equivalent damping ratio ζ_e with frequency correction is set to $1/\sqrt{2}$ here, i.e.,

$$\zeta_e = \frac{B_e}{2\sqrt{JN_p K_\theta}} = \frac{1}{\sqrt{2}}. \tag{32}$$

Substituting (31) into (32), the frequency correction gain k_{dp} is expressed as

$$k_{dp} = \sqrt{\frac{2J}{N_p K_\theta}}. \tag{33}$$

Furthermore, it is necessary to obtain the derivative of motor frequency. According to active power equation, the motor frequency satisfies $\omega_e = P/T_e$. Since the angle error is kept to be zero and the current amplitude I_m is set to its rated value I_n, the torque T_e is nearly constant during startup. Therefore, the derivative of motor frequency $d\omega_e/dt$ is proportional to the derivative of active power dP/dt. According to Fig. 4, the motor oscillation frequency is very low, only several hertz. In low frequency, high-pass filter (HPF) is almost a differentiator. Therefore, the derivative of motor frequency can be obtained by filtering active power P through HPF and the equation is expressed as

$$\frac{d}{dt}\omega_e = \frac{d}{dt}\left(\frac{P}{T_e}\right) \approx \frac{\text{HPF}\,(P)}{T_e}. \tag{34}$$

The active power P and output torque T_e can be estimated by the following equations:

$$P \approx [u_a\ u_b\ u_c]\begin{bmatrix} i_a \\ i_b \\ i_c \end{bmatrix} = \left(\mathbf{M}_{\alpha\beta 2abc}\begin{bmatrix} u_\alpha \\ u_\beta \end{bmatrix}\right)^{\mathrm{T}}\left(\mathbf{M}_{\alpha\beta 2abc}\begin{bmatrix} i_\alpha \\ i_\beta \end{bmatrix}\right)$$
$$= [u_\alpha\ u_\beta]\left(\mathbf{M}_{\alpha\beta 2abc}^{\mathrm{T}}\mathbf{M}_{\alpha\beta 2abc}\right)\begin{bmatrix} i_\alpha \\ i_\beta \end{bmatrix} = 1.5\,[u_\alpha\ u_\beta]\begin{bmatrix} i_\alpha \\ i_\beta \end{bmatrix} \tag{35}$$

$$T_e = 1.5 N_p \lambda_f I_n \tag{36}$$

where the $\mathbf{M}_{\alpha\beta 2abc}$ is the inverse Clark transform matrix, satisfying $\mathbf{M}_{\alpha\beta 2abc} = \begin{bmatrix} 1 & -1/2 & -1/2 \\ 0 & \sqrt{3}/2 & -\sqrt{3}/2 \end{bmatrix}^{\mathrm{T}}$.

Therefore, the active power perturbation gain k_ω in Fig. 9 satisfies

$$k_\omega = \frac{k_{dp}}{T_e} = \frac{2}{3N_p\lambda_f I}\sqrt{\frac{2J}{N_p K_\theta}}. \tag{37}$$

B. Acceleration Controller Design

During speed up stage, i.e., when current vector frequency ω_{i0} is less than set frequency ω_{ref}, the current vector amplitude I is set to rated value I_n to ensure a relatively large startup torque. According to previous analysis, when the load torque T_L is large, the current vector acceleration β_i should be smaller to avoid losing synchronization. When the load torque T_L is small, the current vector acceleration β_i should be larger to shorten the startup time. Therefore, the acceleration β_i should be automatically adjusted as a function of the load torque T_L. With the proposed angle controller, the angle error can be maintained as zero, and the motor frequency ω_e is close to the current vector frequency ω_i. Combining torque (8) and motion (9), the relationship between load torque T_L and current vector acceleration β_i satisfies

$$T_e = \frac{3}{2}N_p\lambda_f I_n = T_L + \frac{J}{N_p}\beta_i + \frac{B}{N_p}\omega_i. \tag{38}$$

It is clear that when the output torque is constant and relatively large, the acceleration β_i is able to adjust automatically with the load torque T_L and is relatively large on the premise of avoiding losing synchronization. Therefore, during speed up stage, maintaining zero angle error θ_{err} ensures large startup torque, short startup time and avoids losing synchronization.

According to γ-axis voltage (5), the angle error θ_{err} can be estimated as

$$\theta_{\text{err}} \approx \sin\theta_{\text{err}} = \frac{-\omega_i L_q i_\delta - u_\gamma}{\omega_e\lambda_f} \approx \frac{-\omega_i L_q i_\delta - u_\gamma}{\omega_i\lambda_f}. \tag{39}$$

The angle error θ_{err} is assumed as $\sin\theta_{\text{err}}$ because it is small due to rotor position initialization and zero angle error controller as analyzed before. The motor frequency ω_e can be approximated as the current vector frequency ω_i. Actually, the speed error ω_e-ω_i determines the derivative of angle error θ_{err} according to (7). Since the angle error θ_{err} fluctuates very little after frequency correction as shown in Fig. 6, the speed error is relatively small.

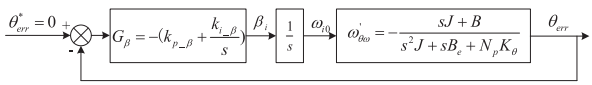

Fig. 11. Small-signal current acceleration closed loop control diagram.

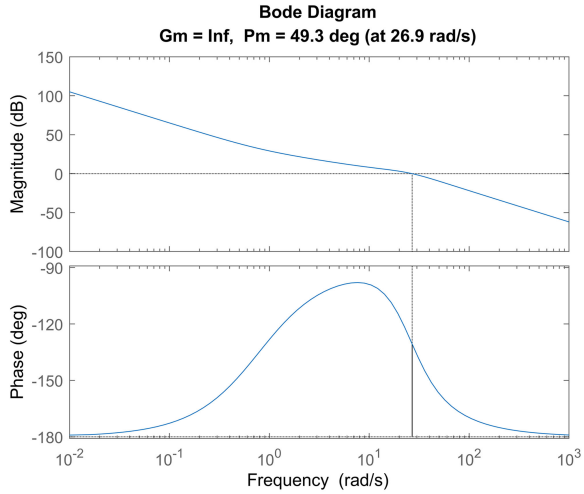

Fig. 12. Bode diagram of current acceleration open loop transfer function.

After obtaining angle error, the acceleration controller adjusts the current vector acceleration β_i. The current vector frequency ω_{i0} obtained from the integration of acceleration β_i affects the angle error θ_{err} through transfer function $G'_{\theta\omega}$ to make the angle error θ_{err} near zero. The small-signal current acceleration closed loop control diagram is shown in Fig. 11. The acceleration controller here uses a robust PI controller to track the reference value θ^*_{err} without steady-state error.

The open loop transfer function $G_{\text{open\_}\beta}$ of acceleration control system is

$$G_{\text{open\_}\beta} = \frac{1}{s}\,G_\beta G'_{\theta\omega} = \frac{1}{s}\left(k_{p\_\beta} + \frac{k_{i\_\beta}}{s}\right)\frac{sJ + B}{s^2J + sB_e + N_pK_\theta}. \tag{40}$$

Considering that the initial angle error θ_{err} at the starting moment may not be close to zero, the acceleration control loop bandwidth should be set smaller to ensure normal startup. In this case, it is set to 4 Hz, which is 1% of the bandwidth of current control loop and the phase margin is about 50°. Fig. 12 shows the Bode diagram of current acceleration open loop transfer function $G_{\text{open\_}\beta}$.

C. Amplitude Controller Design

During speed up stage, once the current vector frequency ω_{i0} is greater than the set frequency ω_{ref}, the current vector frequency ω_{i0} is maintained as the set value ω_{ref} and thus the motor switches to constant speed stage. As analyzed before, in order to improve efficiency, the motor current needs to be reduced to maintain zero angle error θ_{err}.

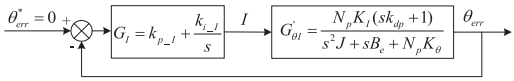

Fig. 13. Small-signal current amplitude closed loop control diagram.

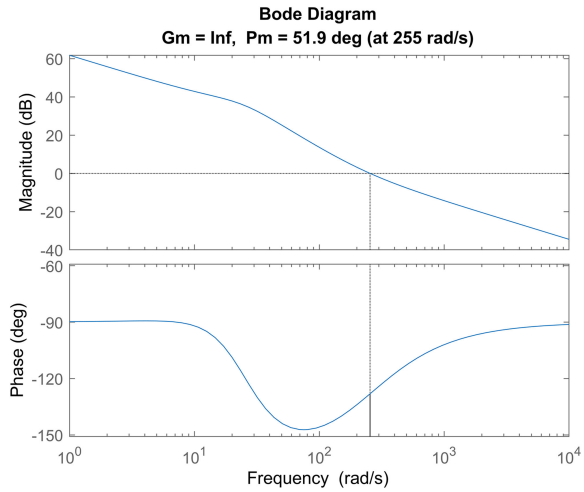

Fig. 14. Bode diagram of current amplitude open loop transfer function.

Similarly, the small-signal current amplitude closed loop control diagram is shown in Fig. 13, including a robust amplitude PI controller.

The open loop transfer function $G_{\text{open\_}I}$ of amplitude control system is

$$G_{\text{open\_}I}=G_IG'_{\theta I}=\left(k_{p\_I}+\frac{k_{i\_I}}{s}\right)\frac{N_pK_I(sk_{dp}+1)}{s^2J+sB_e+N_pK_\theta}. \tag{41}$$

During speed up stage, the angle error θ_{err} is near zero because of the acceleration controller, making it possible to allow transition from speed up stage to constant speed stage smoothly. So the bandwidth of amplitude control loop can be set larger to improve dynamic performance. Therefore, in this case, the bandwidth of amplitude control loop is set to 40 Hz, which is 10% of the bandwidth of current control loop with a phase margin of about 50 °. Fig. 14 shows the Bode diagram of current amplitude open loop transfer function $G_{\text{open\_}I}$.

D. Angle Controller Verification by Large-Signal Model

Combining the large-signal motion model in Fig. 2 and the proposed *I–f* startup method in Fig. 9, the large-signal motion model under *I–f* control with current angle controller can be derived as shown in Fig. 15. The speed, current and angle error waveforms under *I–f* control with angle controller at different loads obtained from large-signal model simulation are recorded in Fig. 16 . It can be seen that the motor starts normally under no load, half load and even full load. Moreover, the proposed *I–f* startup method with angle controller does not need to set the acceleration in advance, because the acceleration adjusts automatically with the changing load. The acceleration is large at light load for faster startup and is small at heavy load, optimizing the tradeoff between startup speed and load capacity. Compared

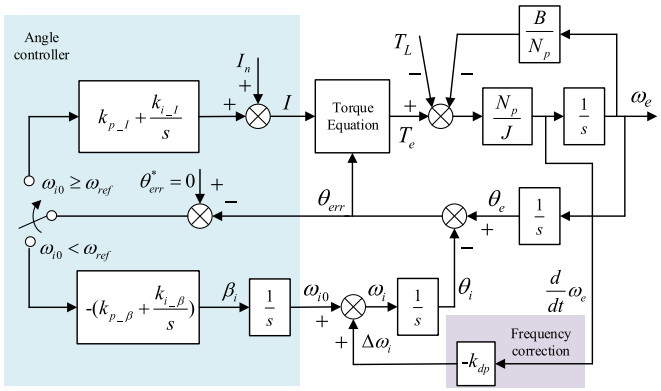

Fig. 15. Large-signal motion model under *I–f* control with angle controller.

with the simulation results of the *I–f* startup method without angle controller in Fig. 6, the angle error θ_{err} of the proposed method with current angle controller is relatively small during the complete startup process, including speed up stage and constant speed stage. In particular, the angle error is close to zero at full load. Under zero angle error control, the q-axis current i_q is close to current amplitude I_m and the d-axis current i_d is relatively small especially in constant speed stage due to high bandwidth of amplitude control loop, which means $i_d=0$ control is achieved. Small angle error ensures high operating efficiency, high output torque and fast startup speed. The simulation results also verify the reasonableness of previous parameter design of frequency correction, acceleration controller and amplitude controller.

V. Robustness Analysis

In order to verify the robustness of the proposed current angle controller, the impact of parameter variations on estimated angle error θ_{err}^{e} is quantified. According to (39), the estimated angle error θ_{err}^{e} is expressed as

$$\theta_{\text{err}}^{e}=\frac{-\omega_iL_q^ei_\delta-u_\gamma}{\omega_i\lambda_f^e} \tag{42}$$

where L_q^e is the estimated value of q-axis inductance and λ_f^e is the estimated value of flux linkage.

Since ω_i and i_δ are the given frequency and amplitude of current vector and u_γ is the output of current regulator, these values can be obtained accurately. Therefore, the parameters that actually affect the estimated angle error θ_{err}^{e} are only estimated inductance L_q^e and estimated flux linkage λ_f^e. Comparing (39) and (42), the relationship between actual angle error θ_{err} and its estimated value θ_{err}^{e} satisfies

$$\theta_{err}=\frac{\lambda_f^e}{\lambda_f}\theta_{\text{err}}^{e}+\left(L_q^e-L_q\right)\frac{i_\delta}{\lambda_f}. \tag{43}$$

When the estimated inductance value L_q^e is equal to its actual value L_q, (43) can be simplified as

$$\theta_{\text{err}}=\frac{\lambda_f^e}{\lambda_f}\theta_{\text{err}}^{e}. \tag{44}$$

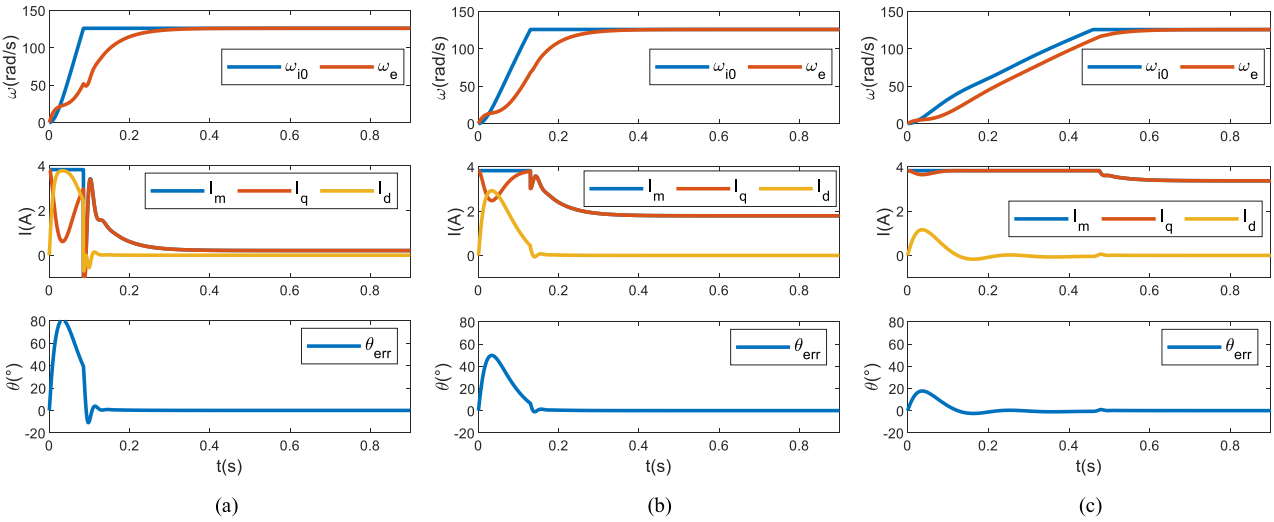

Fig. 16. Simulation results under *I–f* control with angle controller at different loads. From top to bottom: speed, current amplitude, angle error.

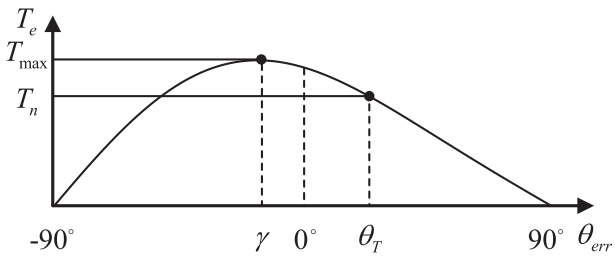

Fig. 17. Variation of generated torque with angle error at rated current.

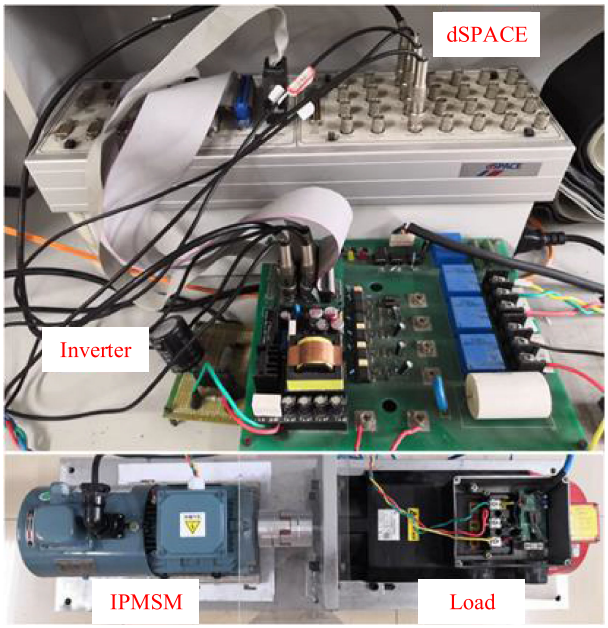

Fig. 18. Experimental platform.

In this case, the actual angle error θ_{err} is proportional to its estimated value θ_{err}^e. Refer to Fig. 9, the estimated input error of angle controller is proportional to its actual value with a multiplier gain of $\frac{\theta_{\text{err}}}{\theta_{\text{err}}^e} = \frac{\lambda_f^e}{\lambda_f}$. As long as the angle controller is reasonably designed, i.e., the system phase margin is relatively large, the system can work properly. It means that the impact of inaccurate estimated flux value λ_f^e is relatively small.

When the estimated flux value λ_f^e is equal to its actual value λ_f, (43) can be simplified as

$$\theta_{\text{err}} = \theta_{\text{err}}^e + \left(L_q^e - L_q\right)\frac{i_\delta}{\lambda_f}. \tag{45}$$

In this case, there is a dc bias between actual angle error θ_{err} and its estimated value θ_{err}^e. Assuming that the angle controller can work properly, the estimated angle error θ_{err}^e will be near zero, so the actual steady-state angle error θ_{err} satisfies

$$\theta_{\text{err}} = \left(L_q^e - L_q\right)\frac{i_\delta}{\lambda_f}. \tag{46}$$

Obviously, the larger the current vector amplitude i_δ is, the larger the absolute value of angle error $|\theta_{\text{err}}|$ will be. Therefore, considering the case with the largest absolute value of angle error, i.e., when the current vector amplitude i_δ is set to the rated current value I_n, the variation of output torque with angle error is recorded in Fig. 17.

In order to avoid losing synchronization, as previously analyzed, the angle error θ_{err} needs to be greater than MTPA angle γ. In addition, the output torque T_e must be at least greater than the rated load T_n to ensure smooth startup under maximum load. When the output torque T_e equals to the rated load T_n, the angle error is marked as load angle θ_T, which satisfies

$$T_n = 1.5N_p I_n \cos\theta_T \left[\lambda_f + \left(L_d - L_q\right) I_n \sin\theta_T\right],\ \theta T > 0. \tag{47}$$

So, the actual angle error θ_{err} needs to meet

$$\gamma < \theta_{\text{err}} < \theta_T. \tag{48}$$

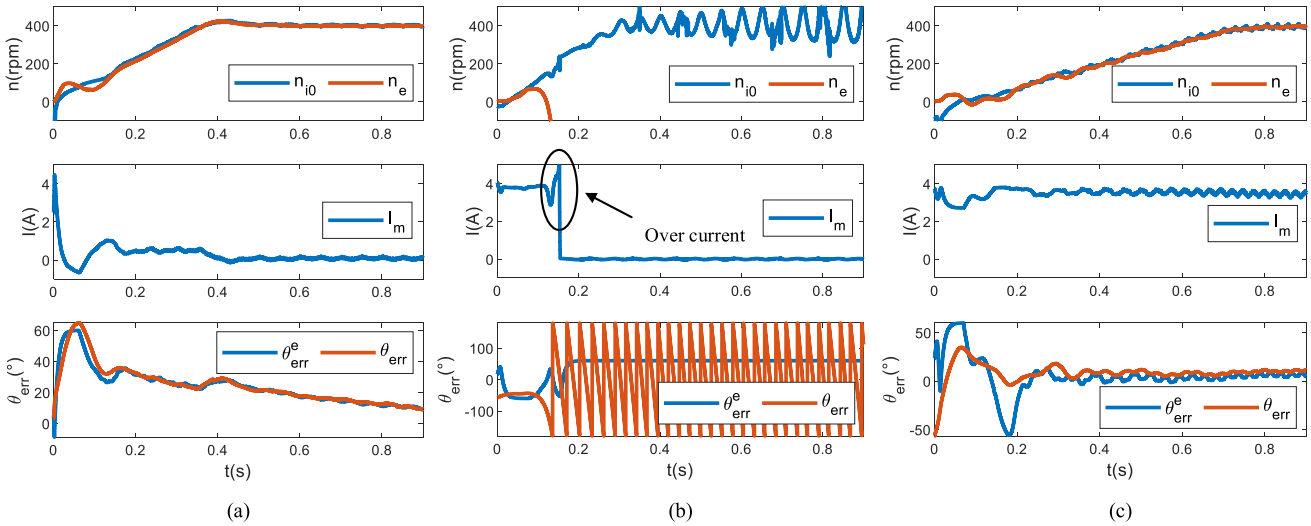

Fig. 19. Experimental results under existing *I–f* control with frequency correction and amplitude controller at different conditions. From top to bottom: speed; current amplitude; angle error. (a) High acceleration and no load. (b) High acceleration and full load. (c) Low acceleration and full load.

Substituting (46) into (48), the range of estimated inductance L_q^e can be obtained as

$$1 + \frac{\lambda_f}{L_q I_n}\gamma < \frac{L_q^e}{L_q} < 1 + \frac{\lambda_f}{L_q I_n}\theta_T. \tag{49}$$

Combined with the motor parameters in Table I, the estimated inductance value at rated current should satisfy

$$44.3\% < \frac{L_q^e}{L_q} < 168\%. \tag{50}$$

It can be seen that the estimated inductance value L_q^e can vary over a wide range without any performance degradation.

When the estimated flux and inductance are different than their actual values, the actual angle error in (43) can be rearranged as follows:

$$\theta_{\text{err}} = \frac{\lambda_f^e}{\lambda_f}\left[\theta_{err}^e + \frac{\lambda_f}{\lambda_f^e}\left(L_q^e - L_q\right)\frac{i_\delta}{\lambda_f}\right]. \tag{51}$$

In fact, the actual angle error is linear to its estimated value, which is a synthesis of the above two cases. Similarly, the effect of gain $\frac{\lambda_f^e}{\lambda_f}$ can be neglected due to the robustness of PI controller, and the motor is still stable as long as the dc bias $\frac{\lambda_f}{\lambda_f^e}(L_q^e - L_q)\frac{i_\delta}{\lambda_f}$ is within a certain range, i.e., greater than MTPA angle γ and less than load angle θ_T.

In summary, the proposed *I–f* startup strategy with current angle controller has a strong robustness performance.

VI. Experimental Results

In order to validate the proposed strategy, the experiments are carried out on the test platform as shown in Fig. 18, including dSPACE controller, inverter, load motor and the tested IPMSM. The parameters of this IPMSM are given in Table I. The switching frequency and control frequency are both at 4 kHz.

A. Performance of Existing I–f Startup Strategy

The existing *I–f* startup strategy [28] adopts frequency correction and amplitude controller with a preset and constant acceleration during speed up stage. It is noteworthy that the amplitude controller is used in speed up stage for higher efficiency and used in constant speed stage for subsequent transition to FOC. The experimental waveforms under high acceleration and no load condition are recorded in Fig. 19(a). After implementing the frequency correction algorithm, there is basically no oscillation during startup. Because of the amplitude controller, the current amplitude I_m and angle error θ_{err} are relatively small throughout the whole process. However, when the motor starts at full load with faster acceleration, the motor loses synchronization and the results are recorded in Fig. 19(b). According to (11), the demand torque T_d is very large under high acceleration and high load condition. Once the demand torque T_d is greater than the maximum output torque $T_{\max}$, the motor will be out of step and the motor current will increase dramatically until the overcurrent protection is triggered. Using this strategy, in order to start smoothly even at full load, the acceleration is usually set to a very small value to meet $T_d < T_{\max}$, and the corresponding results are recorded in Fig. 19(c). Therefore, the existing *I–f* startup strategy needs to set a slower acceleration to ensure smooth startup at full load, which degrades the startup speed performance. In this case, the acceleration is set to be a constant and low value, and it cannot be adjusted automatically with the actual load, which means the acceleration is very small even under light load for successful startup.

B. Performance of Proposed I–f Startup Strategy

To demonstrate large startup torque, high efficiency capability of the proposed *I–f* startup strategy with current angle controller, the experimental results under different load conditions are recorded in Fig. 20. Regardless of at no load, half load or full load, the motor starts smoothly. Moreover, the proposed method

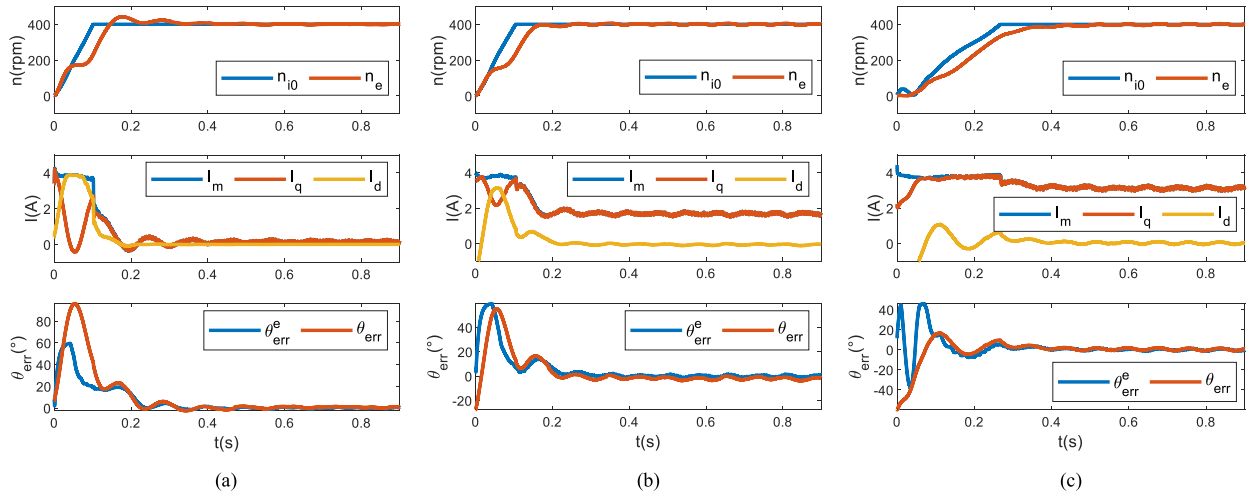

Fig. 20. Experimental results under proposed *I–f* control with angle controller at different loads. From top to bottom: speed; current amplitude; and angle error. (a) No load. (b) Half rated load. (c) Rated load.

does not need to set the startup acceleration in advance, and the acceleration can be adjusted automatically with any varying load. The acceleration is high at light load for fast startup and is low at heavy load. During speed up stage, the current amplitude I_m is large and constant for a large output torque. During constant speed stage, the current amplitude I_m is adjusted with load for high efficiency. After the algorithm runs for 0.1 s, the estimated angle error θ^e_{err} is very close to its actual value θ_{err}, which verifies the accuracy of angle error estimation (39). Throughout the whole process, the angle error θ_{err} is near zero, which validates the effectiveness of this current angle controller. Accordingly, the q-axis current i_q is close to current amplitude I_m and the d-axis current i_d is relatively small especially in constant speed, which means $i_d = 0$ control is achieved. In addition, the experimental waveforms in Fig. 20 are basically consistent with the simulation results in Fig. 16, which validates the precision of the large signal model.

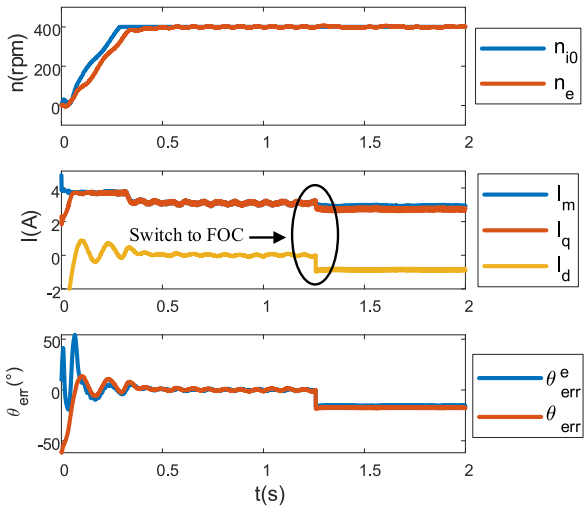

Fig. 21. Experimental results of transition from *I–f* startup to FOC at rated load.

C. Transition From I–f Startup to FOC

In this experiment, the motor starts at rated load and then maintains a constant speed of 400 r/min. When the motor reaches its steady state operation, the control strategy switches from *I–f* startup to FOC as illustrated in Fig. 21. At the switching moment 1.25 s, the d-axis current i_d decreases from zero to a negative value because the $i_d = 0$ operation under *I–f* startup switches to MTPA operation under sensorless FOC. However, the current amplitude I_m decreases slightly and the speed remains basically unchanged, which means the switching transition process from *I–f* startup strategy to sensorless FOC is pretty smooth with zero angle error θ_{err}.

In addition, this transition strategy is simple: First, set the initial reference torque of the speed loop output in the FOC strategy to the output torque of *I–f* control. Second, adopt the dq-axis current references based on reference torque and MTPA strategy rather than *I–f* control. Third, use the angle estimated by the sensorless method to replace the current vector angle given in the *I–f* startup strategy.

D. Robustness Test

According to previous analysis, the electrical parameters used in the proposed *I–f* startup strategy for estimating angle error only contain flux linkage λ_f and q-axis inductance L_q. As these parameters vary, the sensitivity tests are conducted to demonstrate the robustness of proposed strategy. When the motor starts at full load, the current amplitude is larger, the motor is easier to lose synchronization, i.e., the angle error range of successful startup becomes smaller according to Fig. 17. Therefore, the robustness tests are carried out at rated load.

The experimental waveforms at rated load under different estimated flux linkages are captured in Fig. 22. Regardless when $\lambda^e_f = 50\%\lambda_f$ or $\lambda^e_f = 150\%\lambda_f$, the motor is able to start smoothly. In order to analyze the effect of the estimated flux linkage λ^e_f on estimated angle error θ^e_{err}, only the time after the algorithm convergence, i.e., the period $t > 0.1\ s$ is considered. When $\lambda^e_f = 50\%\lambda_f$, according to (44), the angle error $\theta_{\text{err}} = 0.5\theta^e_{\text{err}}$, so the absolute value of angle error $|\theta_{\text{err}}|$ is less

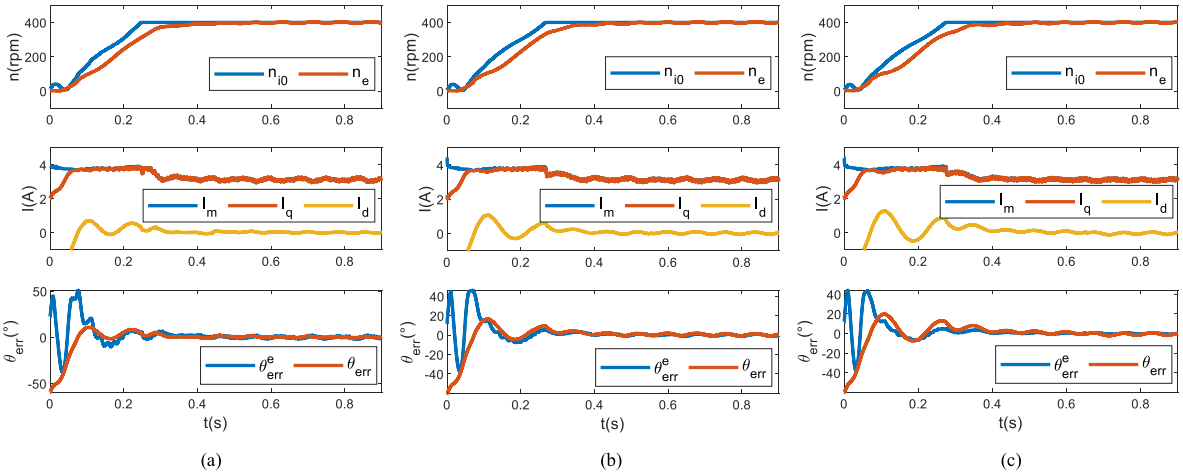

Fig. 22. Experimental results at rated load under different estimated flux linkages. From top to bottom: speed; current amplitude; and angle error. (a) $\lambda_f^e = 50\%\lambda_f$. (b) $\lambda_f^e = 100\%\lambda_f$. (c) $\lambda_f^e = 150\%\lambda_f$

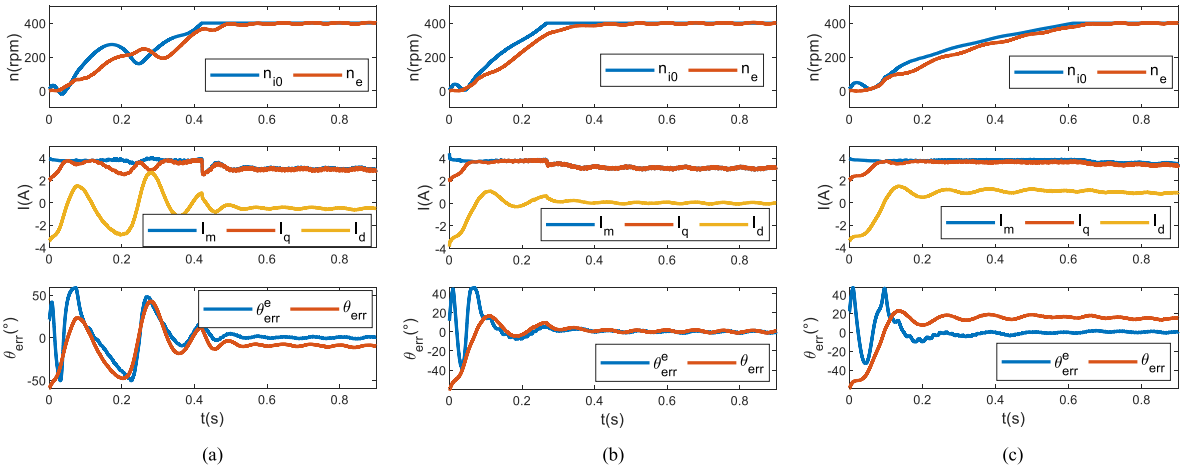

Fig. 23. Experimental results at rated load under different estimated q-axis inductances. From top to bottom: speed; current amplitude; and angle error. (a) $L_q^e = 70\%\ L_q$. (b) $L_q^e = 100\%\ L_q$. (c) $L_q^e = 130\%\ L_q$

than the estimated absolute value $|\theta_{\text{err}}^e|$ as shown in Fig. 22(a). Similarly, when $\lambda_f^e = 150\%\lambda_f$, the angle error $\theta_{\text{err}} = 1.5\theta_{\text{err}}^e$ and in Fig. 22(c) $|\theta_{\text{err}}|$ is greater than $|\theta_{\text{err}}^e|$. In other words, when the estimated flux linkage is not accurate, the actual angle error θ_{err} is proportional to its estimated value. It is equivalent to the case where the gain of angle controller changes. As long as the current angle controller is reasonably designed and the system phase margin is relatively large, the system can work properly, even when the estimated flux linkage λ_f^e varies in the range of $\pm 50\%$.

For different estimated q-axis inductance L_q^e at rated load, the experimental results are presented in Fig. 23. Regardless of when $L_q^e = 70\%\ L_q$ or $L_q^e = 130\% L_q$, the motor starts successfully. According to (45), the angle error $\theta_{\text{err}} = \theta_{\text{err}}^e \mp \frac{0.3 L_q I_\delta}{\lambda_f}$, so there is a dc bias between the actual angle error θ_{err} and its estimated value θ_{err}^e in the experiments. The proposed current angle controller is able to make the estimated angle error θ_{err}^e near zero, so the steady-state angle error is primarily $\theta_{\text{err}} = \mp\frac{0.3 L_q I_\delta}{\lambda_f}$. According to above analysis (48), as long as the angle error θ_{err} is greater than MTPA angle γ and smaller than load angle θ_T, the motor is able to start smoothly. Besides, when $L_q^e < L_q$, the steady-state angle error θ_{err} is less than zero and moves towards MTPA angle γ, reducing the angle margin and thus causing slight oscillation as shown in Fig. 23(a). When $L_q^e > L_q$, the angle error θ_{err} is larger than zero and moves towards load angle θ_T, reducing the output torque and thus increasing the startup time as shown in Fig. 23(c). The analysis is consistent with Fig. 17.

In summary, the proposed *I–f* startup strategy has strong robustness in the presence of electrical parameters variation including flux linkage λ_f and q-axis inductance L_q.

VII. Conclusion

In this article, an efficient *I–f* control with large startup torque is introduced by autoadjusting the current vector acceleration first and then amplitude with varying load using the proposed current angle controller. The proposed angle controller input is the angle error between current vector and q-axis, which can be easily obtained through current oriented voltage equation.

Furthermore, the large-signal motion model is derived for evaluating *I–f* startup performances, while the small-signal motion model is derived for designing controller parameters. The proposed current angle controller is validated through experimentation. The advantages are summarized as follows.

1) During speed up stage, the proposed angle controller adjusts acceleration with any load automatically to maintain zero angle error, which ensures full-load startup with as large startup torque as possible, while maintaining system stability.
2) During constant speed stage, the proposed current angle controller reduces the current amplitude until the angle error reaches zero, which improves efficiency significantly and ensures subsequent smooth transition from *I–f* startup to sensorless FOC.
3) The proposed *I–f* control has strong robustness against parameters variation, achieving full-load startup capability with $\pm 50\% \lambda_f$ and $\pm 30\% L_q$ parameters variation.

REFERENCES

[1] C. J. V. Filho, D. Xiao, R. P. Vieira, and A. Emadi, "Observers for high-speed sensorless PMSM drives: Design methods, tuning challenges and future trends," *IEEE Access*, vol. 9, pp. 56397–56415, 2021.

[2] Y. Han, C. Gong, Z. Ma, C. Liu, W. Li, and G. Chen, "Precise cumulative error calibration with delay effects rejected for incremental encoders used in high-speed PMSMs," *IEEE Trans. Ind. Electron.*, vol. 69, no. 9, pp. 9667–9672, Sep. 2022.

[3] S. Chen, Y. Zhao, H. Qiu, and X. Ren, "High-Precision rotor position correction strategy for high-speed permanent magnet synchronous motor based on resolver," *IEEE Trans. Power Electron.*, vol. 35, no. 9, pp. 9716–9726, Sep. 2020.

[4] X. Song, B. Han, S. Zheng, and S. Chen, "A novel sensorless rotor position detection method for high-speed surface PM motors in a wide speed range," *IEEE Trans. Power Electron.*, vol. 33, no. 8, pp. 7083–7093, Aug. 2018.

[5] G. Zhang, G. Wang, B. Yuan, R. Liu, and D. Xu, "Active disturbance rejection control strategy for signal injection-based sensorless IPMSM drives," *IEEE Trans. Transp. Electrific.*, vol. 4, no. 1, pp. 330–339, Mar. 2018.

[6] C. Gong, Y. Hu, J. Gao, Y. Wang, and L. Yan, "An improved delay-suppressed sliding-mode observer for sensorless vector-controlled PMSM," *IEEE Trans. Ind. Electron.*, vol. 67, no. 7, pp. 5913–5923, Jul. 2020.

[7] Y. Zhao, W. Qiao, and L. Wu, "Improved rotor position and speed estimators for sensorless control of interior permanent-magnet synchronous machines," *IEEE J. Emerg. Sel. Top. Power Electron.*, vol. 2, no. 3, pp. 627–639, Sep. 2014.

[8] S. Bolognani, R. Oboe, and M. Zigliotto, "Sensorless full-digital PMSM drive with EKF estimation of speed and rotor position," *IEEE Trans. Ind. Electron.*, vol. 46, no. 1, pp. 184–191, Feb. 1999.

[9] D. Liang, J. Li, R. Qu, and W. Kong, "Adaptive second-order sliding-mode observer for PMSM sensorless control considering VSI nonlinearity," *IEEE Trans. Power Electron.*, vol. 33, no. 10, pp. 8994–9004, Oct. 2018.

[10] J.-H. Jang, S.-K. Sul, J.-I. Ha, K. Ide, and M. Sawamura, "Sensorless drive of surface-mounted permanent-magnet motor by high-frequency signal injection based on magnetic saliency," *IEEE Trans. Ind. Appl.*, vol. 39, no. 4, pp. 1031–1039, Jul. 2003.

[11] Z. Lin, X. Li, Z. Wang, T. Shi, and C. Xia, "Minimization of additional high-frequency torque ripple for square-wave voltage injection IPMSM sensorless drives," *IEEE Trans. Power Electron.*, vol. 35, no. 12, pp. 13345–13355, Dec. 2020.

[12] E. Robeischl and M. Schroedl, "Optimized INFORM measurement sequence for sensorless PM synchronous motor drives with respect to minimum current distortion," *IEEE Trans. Ind. Appl.*, vol. 40, no. 2, pp. 591–598, Mar. 2004.

[13] C. Zhao, M. Tanaskovic, F. Percacci, S. Mariethoz, and P. Gnos, "Sensorless position estimation for slotless surface mounted permanent magnet synchronous motors in full speed range," *IEEE Trans. Power Electron.*, vol. 34, no. 12, pp. 11566–11579, Dec. 2019.

[14] P. D. C. Perera, F. Blaabjerg, J. K. Pedersen, and P. Thogersen, "A sensorless, stable V/f control method for permanent-magnet synchronous motor drives," *IEEE Trans. Ind. Appl.*, vol. 39, no. 3, pp. 783–791, May 2003.

[15] R. Ancuti, I. Boldea, and G.-D. Andreescu, "Sensorless V/f control of high-speed surface permanent magnet synchronous motor drives with two novel stabilising loops for fast dynamics and robustness," *IET Elect. Power Appl.*, vol. 4, no. 3, 2010, Art. no. 149.

[16] A. Consoli, G. Scelba, G. Scarcella, and M. Cacciato, "An effective energy-saving scalar control for industrial IPMSM drives," *IEEE Trans. Ind. Electron.*, vol. 60, no. 9, pp. 3658–3669, Sep. 2013.

[17] Z. Wang, K. Lu, and F. Blaabjerg, "A simple startup strategy based on current regulation for back-EMF-based sensorless control of PMSM," *IEEE Trans. Power Electron.*, vol. 27, no. 8, pp. 3817–3825, Aug. 2012.

[18] F. Haichao, S. Boyang, and G. Lizhen, "A closed-loop I/f vector control for permanent magnet synchronous motor," in *Proc. 9th Int. Conf. Model. Identification Control*, 2017, pp. 965–969.

[19] S. V. Nair, K. Hatua, N. V. P. R. D. Prasad, and D. K. Reddy, "A quick I-f starting of PMSM drive with pole slipping prevention and reduced speed oscillations," *IEEE Trans. Ind. Electron.*, vol. 68, no. 8, pp. 6650–6661, Aug. 2021.

[20] D. Chen, K. Lu, and D. Wang, "An I-f startup method with compensation loops for PMSM with smooth transition," *IEEJ J. Ind. Appl.*, vol. 9, no. 3, pp. 263–270, May 2020.

[21] M. Fatu, R. Teodorescu, I. Boldea, G. Andreescu, and F. Blaabjerg, "I-f starting method with smooth transition to EMF based motion-sensorless vector control of PM synchronous motor/generator," in *Proc. IEEE Power. Electron. Spec. Conf.*, 2008, pp. 1481–1487.

[22] A. Stirban, I. Boldea, and G.-D. Andreescu, "Motion-sensorless control of BLDC-PM motor with offline FEM-information-assisted position and speed observer," *IEEE Trans. Ind. Appl.*, vol. 48, no. 6, pp. 1950–1958, Nov. 2012.

[23] H. Shen and C. Zhang, "A new efficient sensorless I/f control method for IPMSM drives," in *Proc. IEEE 26th Int. Symp. Ind. Electron.*, 2017, pp. 209–213.

[24] Y. Yu, D. Chang, X. Zheng, Z. Mi, X. Li, and C. Sun, "A stator current oriented closed-loop I-f control of sensorless SPMSM with fully unknown parameters for reverse rotation prevention," *IEEE Trans. Power Electron.*, vol. 33, no. 10, pp. 8607–8622, Oct. 2018.

[25] M. Pacha and S. Zossak, "Improved simple I-f open-loop start-up of PMSM drives without speed or position sensor," in *Proc. IEEE 10th Int. Symp. Sensorless Control Elect. Drives*, 2019, pp. 1–6.

[26] J. Xing, Z. Qin, C. Lin, and X. Jiang, "Research on startup process for sensorless control of PMSMs based on I-F method combined with an adaptive compensator," *IEEE Access*, vol. 8, pp. 70812–70821, 2020.

[27] X. Jin, R. Ni, W. Chen, F. Blaabjerg, and D. Xu, "High-frequency voltage-injection methods and observer design for initial position detection of permanent magnet synchronous machines," *IEEE Trans. Power Electron.*, vol. 33, no. 9, pp. 7971–7979, Sep. 2018.

[28] M. Wang, J. Yang, X. Zhang, and C. Zhu, "An I/f control method with closed-loop regulation of current vector for surface permanent magnet synchronous motor drives," *Proc. Chin. Soc. Elect. Eng.,* vol. 35, no. 10, pp. 2513–2521, May 2015.

Zhihao Song (Student Member, IEEE) received the B.S. degree in electrical engineering in 2019 from Zhejiang University, Hangzhou, China, where he is currently working toward the Ph.D. degree in electrical engineering.

His main research interests include sensorless control and high speed PMSM control.

Wenxi Yao (Member, IEEE) received the B.S. and Ph.D. degrees in electrical engineering from Zhejiang University, Hangzhou, China, in 2000 and 2006, respectively.

He is currently an Associate Professor of electrical engineering, Zhejiang University. From 2010 to 2011, he was a Visiting Scholar with FREEDM, North Carolina State University. He has authored or coauthored more than 100 published technical papers. His research interests include multilevel converter and sensorless control of ac motor drives.

Kevin Lee (Fellow, IEEE) received the M.S. degree from Rensselaer Polytechnic Institute, Troy, NY, USA, in 1990, and the Ph.D. degree from University of Wisconsin, Madison, USA in 2008, both in electrical engineering.

In 1998, he was with the Eaton Corporation, where he is a Chief Engineer in Industrial Control Division, responsible for technology and product development in the fields of power quality, energy efficiency, adjustable speed drives, power distribution system architecture and control systems. Prior to joining Eaton, he was an Engineering Manager with Sola/Hevi-Duty Electric, a Unit of General Signal, and an Emerson Industrial Automation, from 1990 to 1998.

Dr. Lee was the recipient of the IEEE Industry Applications Magazine First Prize Paper Award in 2009 and Eaton Engineer of the Year Award in 2013. Since 1995, he has been a Registered Professional Engineer with the State of Wisconsin, a certified Design for Six Sigma Black Belt, and a holder of 41 U.S. patents. He is currently the Standards Sub-Committee Chair and the Vice Chair in Industrial Drives Committee of the IEEE Industry Applications Society.

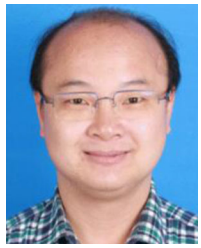

Wuhua Li (Member, IEEE) received the B.Sc. and Ph.D. degrees in applied power electronics and electrical engineering from Zhejiang University, Hangzhou, China, in 2002 and 2008, respectively.

From 2004 to 2005, he was a Research Intern, and from 2007 to 2008, a Research Assistant with GE Global Research Center, Shanghai, China. From 2008 to 2010, he was a Postdoctoral with the College of Electrical Engineering, Zhejiang University. In 2010, he was promoted as an Associate Professor. Since 2013, he has been a Full Professor with Zhejiang University. From 2010 to 2011, he was a Ryerson University Postdoctoral Fellow with the Department of Electrical and Computer Engineering, Ryerson University, Toronto, ON, Canada. He is currently the Vice Dean of the College of Electrical Engineering and the Deputy Director of the National Specialty Laboratory for Power Electronics, Zhejiang University. He has authored/coauthored more than 300 peer-reviewed technical papers and holds more than 50 issued/pending patents. His research interests include power devices, converter topologies, and advanced controls for high-power energy conversion systems.